

Strain-induced two-dimensional topological crystalline insulator

Liwei Jing,¹ Mohammad Amini,^{2,*} Adolfo O. Fumega,^{2,*} Orlando J. Silveira,^{1,2,*} Jose L. Lado,^{2,†} Peter Liljeroth,^{2,†} and Shawulienu Kezilebieke^{1,3,†}

¹*Department of Physics, Nanoscience Center,*

University of Jyväskylä, FI-40014 University of Jyväskylä, Finland

²*Department of Applied Physics, Aalto University, FI-00076 Aalto, Finland*

³*Department of Chemistry, University of Jyväskylä,*

FI-40014 University of Jyväskylä, Finland

(Dated: October 10, 2024)

Topological crystalline insulators (TCIs) host topological phases of matter protected by crystal symmetries. Topological surface states in three-dimensional TCIs have been predicted and observed in IV-VI SnTe-class semiconductors. Despite the prediction of a two-dimensional (2D) TCI characterized by two pairs of edge states inside the bulk gap, materials challenges have thus far prevented its experimental realization. Here we report the growth and characterization of bilayer SnTe on the 2H-NbSe₂ substrate by molecular beam epitaxy and scanning tunneling microscopy. We experimentally observe two anticorrelated, periodically modulated pairs of conducting edge states along the perimeters of the sample with a large band gap exceeding 0.2 eV. We identify these states with a 2D TCI through first principles calculations. Finally, we probe the coupling of adjacent topological edge states and demonstrate the resulting energy shift driven by a combination of electrostatic interactions and tunneling coupling. Our work opens the door to investigations of tunable topological states in 2D TCIs, of potential impact for spintronics and nanoelectronics applications at room temperature.

I. INTRODUCTION

Topological insulators (TIs) feature an energy gap in the bulk and nontrivial surface or edge states that connect the valence and conduction bands¹⁻³. The discovery of quantum spin Hall (QSH) effect in HgTe/CdTe quantum wells⁴ has sparked intensive research on novel topological materials extending from three-dimensional (3D) to two-dimensional (2D) systems⁵⁻¹⁰. Meanwhile, crystal symmetries are discovered to play an analogous role as time-reversal symmetry of QSH insulators, which can protect the boundary states from backscattering and thus result in dissipationless carrier transport¹¹. Unlike QSH described by Z_2 invariant, the topology in topological crystalline insulators (TCIs) is classified by the finite Chern number in each symmetry sector, having a net zero total Chern number. 3D TCIs have been realized in semiconductors tin telluride (SnTe)^{12,13}, $\text{Pb}_{1-x}\text{Sn}_x\text{Se}$ ^{14,15}, and $\text{Pb}_{1-x}\text{Sn}_x\text{Te}$ ^{16,17}, in which topological surface states are highly dependent on the surface orientations depending on whether time-reversal-mirror symmetry is broken or preserved. If the time-reversal-mirror symmetry with respect to the (110) bulk mirror plane is broken, the Dirac cones would acquire a band gap and Dirac fermions would obtain mass^{14,18}. The (001) SnTe films are predicted to be 2D TCIs both in the single atomic layer (AL) limit¹⁹ and above 5 ALs²⁰. They should host two pairs of edge states protected by the time-reversal-mirror symmetry $z \rightarrow -z$ (z is normal to the film) through a nonzero time-reversal-mirror Chern number.

The hallmark of a 2D TCI is the presence of metallic edge states along the sample boundary. Higher-order one-dimensional (1D) topological hinge states^{21,22} and surface step edge states²³ have been theoretically predicted and experimentally observed, but it remains a challenge to realize a strong 2D TCI with a wide band gap due to the complicated fabrication of thin films and strong substrate-induced hybridization effects. Particularly, only the odd number of ALs are expected to be 2D TCIs because they keep the symmorphic crystal symmetry with non-zero time-reversal-mirror Chern number^{12,24}. However, each monolayer of (001) SnTe ultrathin films in the rock-salt structure contains 2 ALs and thus we always get an even number of ALs in experiments²⁵, which prevents the band inversion necessary for a topological phase transition. Besides, a strong ferroelectric phase also emerges in the ultrathin limit^{26,27}. Realization of a 2D TCI could be achieved with strain, which allows tailoring the electronic band gap and electronic phase transitions of few-AL SnTe films²⁸.

In this work, we utilize epitaxial growth to fabricate bilayer SnTe (4 ALs) islands on the bulk $2H\text{-NbSe}_2$ and investigate atomic-scale structure and electronic properties using low-temperature scanning tunneling microscopy (STM) and spectroscopy (STS). We experimentally observe strong

edge modes that can be rationalized through density functional theory (DFT) calculations showing the top 3 ALs of SnTe are decoupled from the first 1 AL due to strong interfacial interactions. The concomitant strain drives our effective 3-AL system to undergo a crossover from trivial ferroelectricity to a TCI phase. Finally, we probe experimentally the coupling of edge states from adjacent bilayer SnTe islands and reveal significant energy shifts. Our study highlights a pathway for creating strain-induced emergent quantum states of matter, which could significantly impact energy-efficient electronics.

II. RESULTS

A. Experimental realization of strained 3 atomic layers

We prepared ultrathin SnTe films on a $2H$ -NbSe₂ substrate using the molecular beam epitaxy (MBE, see the Methods section for details on sample preparation). Since each monolayer consists of 2 ALs in the rock-salt SnTe structure, the growing island thickness is always an integer multiple of monolayer in ultrathin films. By carefully controlling the growth conditions, we achieved monolayer-by-monolayer growth. As shown in Figure 1a, the monolayer forms large amorphous islands where the bilayer subsequently nucleates. The height profile (see SI Figure S6) confirms that both layers are one monolayer thick. The stripes visible in Fig. 1b extend from the monolayer to the bilayer and they arise from the moiré patterns resulting from large mismatch between the square SnTe lattice (Te-Te distance of 4.5 Å) and the hexagonal $2H$ -NbSe₂ lattice (Se-Se distance of 3.4 Å). Monolayer SnTe islands exhibit a disordered structure with varying stripe orientations, serving as the wetting layer for the bilayer. In addition, the monolayer stripe patterns reflect a periodically varying strain field in the bilayer (see Extended Data in SI Figure S7). The strain field predominantly distributes along strained moiré patterns, with one unit cell of strain field being shown by orange color in Fig. 1c. By fast Fourier transform (in the inset) of atom-resolved bilayer SnTe topography in Fig. 1c, we find the lattice constants along the [100] and [010] directions are approximately 4.17 Å and 4.33 Å, respectively, which indicates bilayer SnTe is biaxially compressed. This scenario is quite different from the stress-free ultrathin SnTe films grown on graphene and graphite^{26,27}.

To understand the 4-AL SnTe/ $2H$ -NbSe₂ heterostructure, we performed DFT calculations. Fig. 1d presents the side view of our heterostructure model after full relaxation (more details in SI Figure S8). The results suggest that strong hybridization between SnTe and $1H$ -NbSe₂ causes Sn

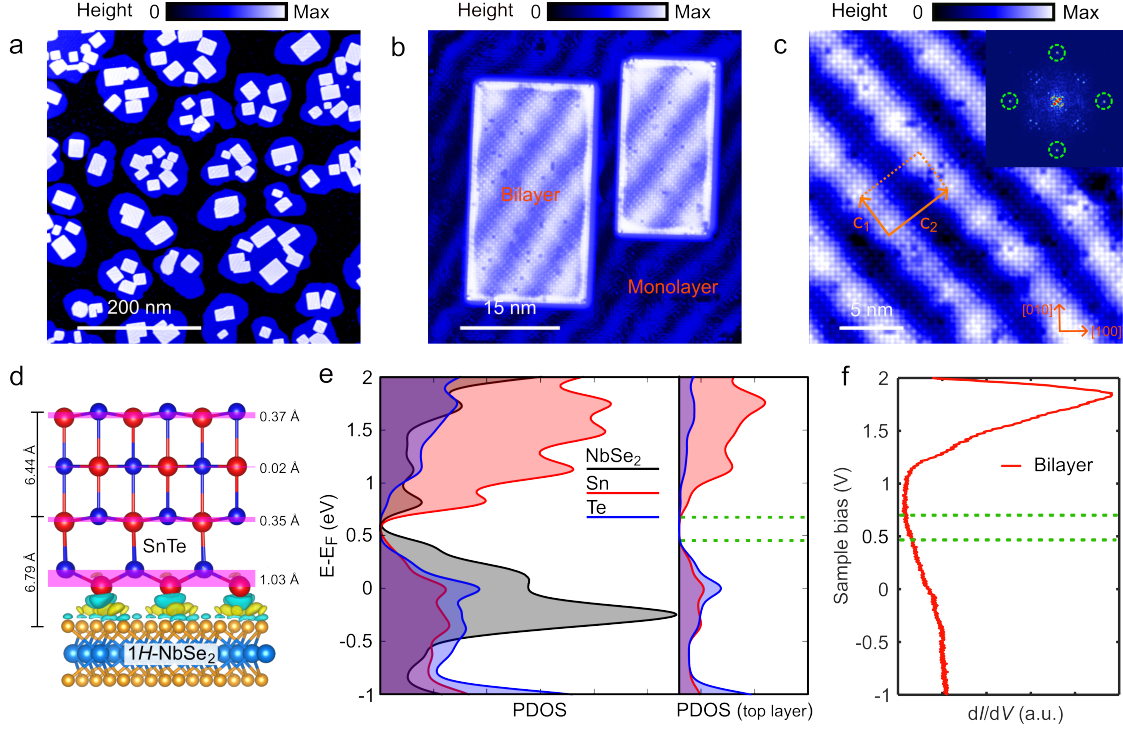


FIG. 1. **Heteroepitaxial bilayer SnTe on 2H-NbSe₂.** **a**, Large-scale STM topographic image of bilayer SnTe on the 2H-NbSe₂ substrate (tunneling parameters: $V_b=1$ V, $I=2.5$ pA). **b**, Typical STM image of bilayer SnTe islands with visible stripe patterns ($V_b=0.8$ V, $I=200$ pA). **c**, Atomic-resolution STM topography of bilayer SnTe islands ($V_b=0.3$ V, $I=230$ pA). Sublattice Sn atoms are aligned along [100] and [010] directions indicated by orange color, which corresponds to a set of Bragg lattice peaks outlined by green dashed circles in the inset. One of strain superlattices is marked by a nearly rectangular frame along c_1 and c_2 directions. **d**, Side view of the heterostructure model of 4-AL SnTe on 1H-NbSe₂ after full relaxation. The charge difference at the interface shown by green and yellow colors reveals that the bottom 1-AL SnTe bonds to the 1H-NbSe₂ underneath through Sn atoms, giving rise to its substantial decoupling from the top 3 ALs. The red, dark blue, orange, and light blue balls represent Sn, Te, Se and Nb atoms, respectively. **e**, Calculated PDOS of bilayer SnTe/1H-NbSe₂ by DFT methods. The left panel shows the PDOS components of all the Sn, Te and NbSe₂ orbitals onto themselves while the right panel displays PDOS of all the Sn and Te orbitals onto the Sn and Te atoms of the topmost atomic layer. **f**, Tunneling differential spectrum taken in the middle of bilayer SnTe. Two pairs of horizontal dashed green lines in **e** and **f** indicate the calculated and experimental bulk band gap edges of bilayer SnTe.

atoms from the bottom 1 AL to be bonded to the substrate. The lattice mismatch further forces the top 3 ALs to be significantly decoupled from the bottom 1 AL with a substantial structural distortion. The interlayer height obtained from the DFT calculations is in good agreement with our experimental data. The projected density of states (PDOS) onto the top 1-AL SnTe is shown in

Fig. 1e. The calculated PDOS agrees well with the experimentally measured tunneling differential spectrum (Fig. 1f), where the bulk band gap edges are marked by green dashed lines. Besides charge transfer with the substrate, Sn vacancies in bilayer SnTe further enhance its pronounced p-type character, lowering the Fermi level below the bulk valence band maximum²⁹. The estimated bilayer bulk band gap ranges between 0.2 and 0.3 eV, depending on the island size. A detailed analysis of the bulk gap can be found in the SI Figure S14. This analysis shows that the experiment effectively realizes a strained 3-AL SnTe system, with a 1-AL wetting layer on the $2H\text{-NbSe}_2$ substrate.

B. Lifshitz transition driven by biaxial strain

We now focus on the theoretical analysis of the topological properties in the effective strained 3-AL SnTe system. As shown in Figure 2a, a 3-AL SnTe structural model has a cubic rock-salt structure with a Sn-Sn spacing of 4.5 Å and preserves the reflection symmetry $z \rightarrow -z$ with respect to the atomic layer in the middle plane (pink shadow). This system hosts two equivalent high-symmetry X points in the 2D Brillouin zone. On the other hand, ultrathin SnTe films are known to spontaneously distort along the $[111]$ direction into a rhombohedral structure and form a ferroelectric phase. This in-plane 2D ferroelectricity does not break the mirror symmetry. This allows for competition between ferroelectricity and a TCI phase. *Ab initio* calculations enable us to establish a phase diagram of the 3-AL SnTe system as a function of biaxial strain. Fig. 2b shows ferroelectric displacement δ_{FE} of this system evolves with the lattice parameter. Above $a \simeq 4.38$ Å, ferroelectric distortion occurs in the xy plane, evidenced by the harmonic phonon spectra (see Extended Data Phonon frequency in SI Figure S5). DFT calculations reveal that the band gap of this system first closes and then reopens at the X point when the lattice constants go through from the tensile to compressive strain, as shown in Fig. 2d. This change in Fermi surface topology corresponds to a Lifshitz transition as a function of in-plane lattice parameter. The gap closing at the X point is the critical point of a phase transition (Fig. 2c), where compressive strain and spin-orbit coupling can induce a band inversion (see Extended Data in SI Figure S3).

The topological phase is protected by the simultaneous combination of time-reversal and mirror symmetries, which in the following we refer to as time-reversal-mirror symmetry. The topological invariant of a strained 3-AL SnTe system can be obtained in the gapped phases by extracting a Wannier Hamiltonian from DFT calculations. The results show that the time-reversal-mirror Chern number vanishes $\mathcal{C}_{\pm M} = 0$ in the tensile regime while the time-reversal-mirror Chern number is

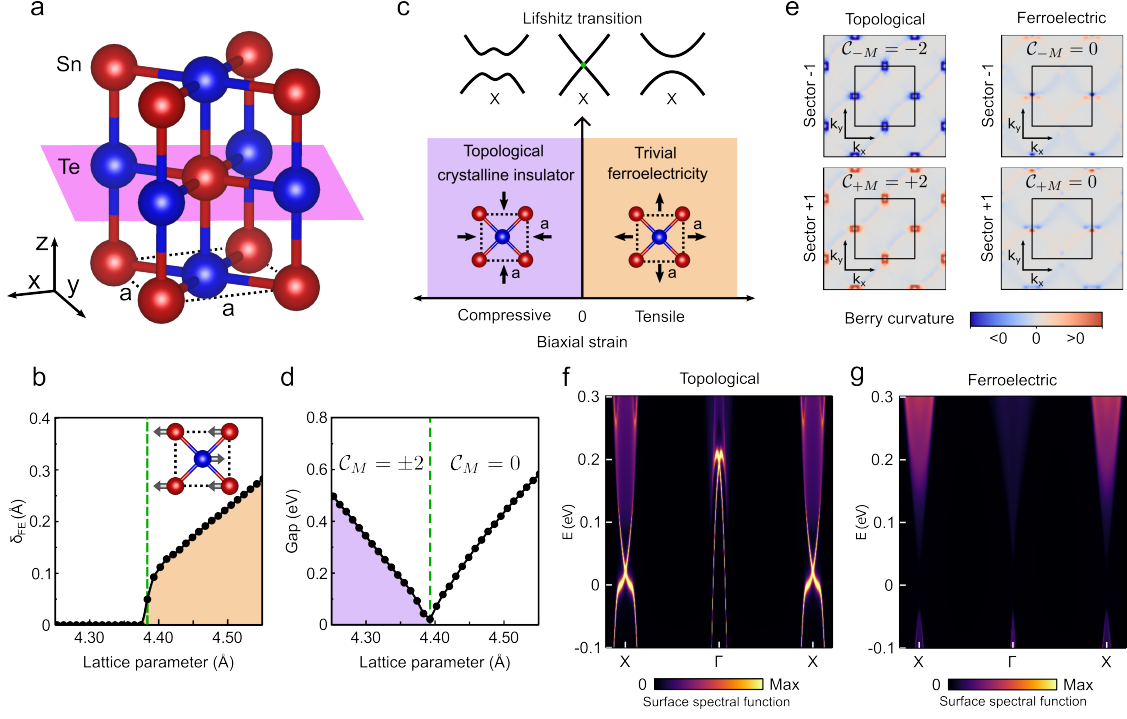


FIG. 2. Crystal structure and band structure of 3-AL SnTe. **a**, Schematic structure of 3-AL SnTe along the (001) orientation, where one mirror plane in the middle of this system from $z \rightarrow -z$ is indicated by a pink shadow. **b**, Ferroelectric displacement δ_{FE} between the cation Sn and anion Te evolves with in-plane lattice parameter, schematically represented at the right-top corner. **c**, Phase diagram of a 3-AL SnTe system as a function of biaxial strain. A Lifshitz transition at the X point takes place when strain goes through from tensile to compressive regime. Correspondingly, the change in Fermi surface topology produces trivial ferroelectric order in tension and a TCI phase in compression. **d**, Evolution of the band gap at the X point with the lattice constant. The closing of the band gap triggers a topological phase transition that can be defined by time-reversal-mirror Chern number \mathcal{C}_M . **e**, Left(right) plots demonstrate the mirror Berry curvature in reciprocal space for a topological (ferroelectric) phase for the -1 (top) and +1 (bottom) mirror sectors, respectively. **f** and **g**, Band structure along X - Γ - X direction for the topological (ferroelectric) phase of a semi-infinite ribbon. Two Dirac points are visible at the X and Γ points for the topological phase.

$\mathcal{C}_{\pm M} = \pm 2$ in the compressive regime (Fig. 2d), signaling the emergence of a TCI phase. This finding is schematically depicted in Fig. 2c. Fig. 2e displays the computed time-reversal-mirror Berry curvature for each of the symmetry sectors (± 1) of the operator $\mathcal{M} = M_{(001)}\Theta$, where $M_{(001)}$ is the (001) mirror and Θ is the time-reversal symmetry operator. In the topological phase, the mirror Berry curvature is well localized around two X points and possesses an opposite sign for each symmetry sector. In the ferroelectric phase, the mirror Berry curvature is not localized and changes

the sign with each symmetry sector, resulting in $\mathcal{C}_{\pm M} = 0$. The bulk-boundary correspondence requires that there must be gapless edge states in the biaxially compressive 3-AL system. The time-reversal-mirror Chern number of ± 2 allows two pairs of Dirac cones located around X points in the 2D Brillouin zone, and with further projection into the specific edges, we obtain two pairs of edge state subbands along the X - Γ - X direction (Fig. 2f). Co-propagating edge states carry identical mirror eigenvalues. At the band crossings at Γ and X points, edge states with opposite mirror eigenvalues propagate in the opposite direction. The two pairs of edge state subbands exhibit linear dispersion around the crossing points, extending into the bulk band gap. In contrast, there are no gapless edge states connecting valence and conduction bands in the ferroelectric phase, as shown in Fig. 2g.

C. Experimental evidence of topological edge states

We present two direct experimental proofs to verify the existence of a 2D TCI in our effective 3-AL system. The first one is that we observe two strong peaks associated to two pairs of edge states extending to the bulk gap along the specific edges of bilayer SnTe islands. As shown in Figure 3a), the dI/dV spectrum taken at the bilayer edge exhibits two pronounced peaks located around 0.5 V (peak 1) and 1.6 V (peak 2). We attribute these peaks to edge states (see SI Figure S10 and S11). These experimental results can be compared with calculations by computing the density of states (DOS) in the bulk and edge of the compressive 3-AL system, where we obtain two sharp peaks with one residing in the bulk gap and the other within the conduction band of bulk states. The low-energy peak at the edge is produced by the substantially enhanced DOS induced by the flatter dispersion of the pair of edge states at the X crossing point (Fig. 2f). Analogously, the high-energy peak at the edge is produced by the enhanced DOS induced by the flatter dispersion of the pair of edge states at the Γ crossing point (Fig. 2f). Therefore, each peak corresponds to the crossing of counter-propagating pairs of edge states. The edge state subbands above the peak 1 are fully within the bulk gap (from 0.5 to 0.7 eV). The discrepancy of the energy peak positions between theory and experiment stems from the typical underestimation of the band gap in DFT calculations.

To resolve the spatial modulation of edge states, we first conduct dI/dV spectroscopy across the opposite edges of a bilayer island (top panel in Fig. 3b). At each edge, there are two edge state peaks located at low and high energies, outlined by the dashed oval frames in the middle panel. These peaks are highly localized around the edges. Similar to the observations in Fig. 3a, the peak

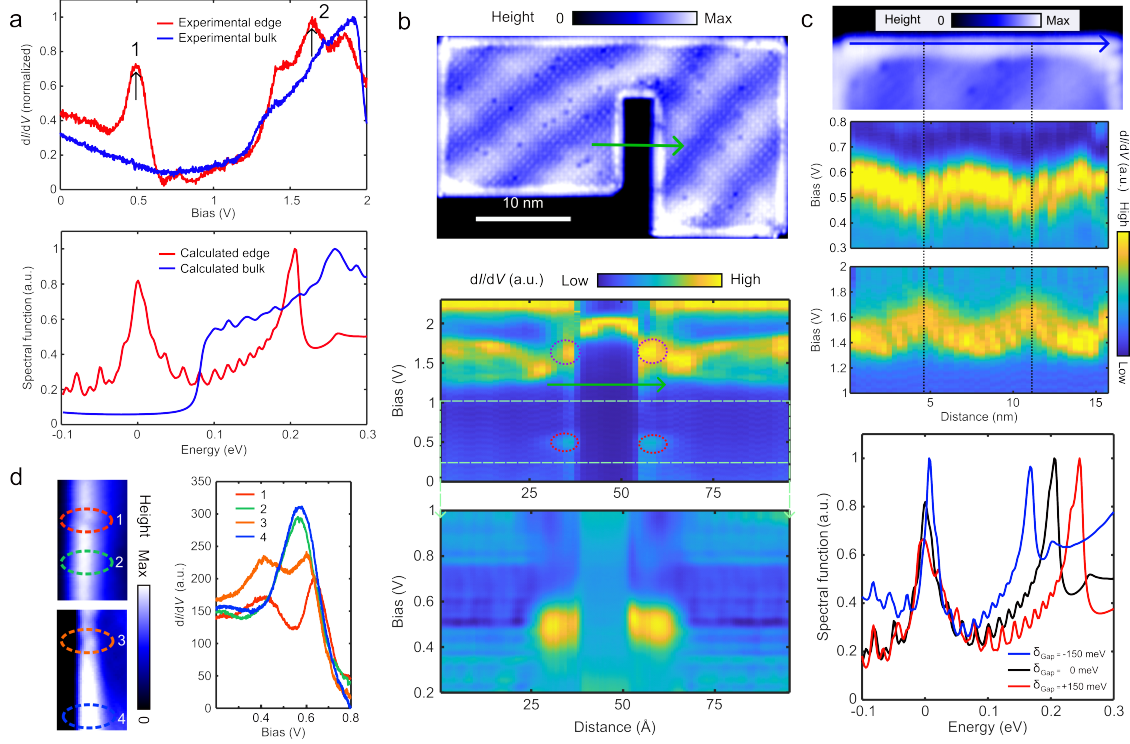


FIG. 3. The topological edge states and their spatial variation. **a**, Tunneling differential spectra taken in the middle and edge of bilayer SnTe on the $2H$ -NbSe₂ (top panel) and calculated spectral function of the bulk and edge in the strained 3-AL system (bottom panel). The spectral function is calculated by integrating all the subbands shown in Fig. 2f for a given energy. **b**, Plots of dI/dV spectra in different energy ranges along the linecut (top panel) are shown in the middle and bottom panel (scan parameters for topography: $V_b=0.8$ V, $I=5$ pA). Two pairs of edge state peaks are highlighted by red dashed oval frames. **c**, Two edge state peaks vary periodically with strained moiré patterns at the edge of bilayer SnTe islands (top and middle panel) ($V_b=0.8$ V, $I=2.2$ pA). They have a π phase difference in spatial variation. We used a phenomenological method to reproduce this result by calculations (bottom panel). δ_{Gap} represents the energy gap between two edge state peaks. **d**, Two typical atomic defects at the edges of bilayer islands are highlighted by red and orange colors and other two ideal sites are also marked by green and blue colors for comparison. Tunneling spectra taken at those positions are shown in the right panel ($V_b=0.8$ V, $I=5$ pA).

1 almost resides the bulk gap (bottom panel) while the peak 2 lies inside the conduction band. It is important to note that the exact energy position of the edge states depends on the strain field, e.g., the strain field can shift the energy of the peak 1 beyond the bulk gap. Series of local DOS (LDOS) oscillations between 0.2 and 1 V as shown in the bottom panel of Fig. 3b are likely to be related to the LDOS oscillations in the SnTe wetting layer or in the NbSe₂ substrate (see further details in the SI Figure S13). We also performed the dI/dV spectroscopy along the blue linecut indicated in Fig. 3c(top panel) and the results show that both the peak 1 and the peak 2 modulate

periodically following the moiré pattern at the island edges (two middle panels). Interestingly, the two peaks are anticorrelated, exhibiting a π phase difference. The energy shift of the peak 2 is approximately 2 times as large as the peak 1. To rationalize these observations, we developed a phenomenological model. Considering that strain induces changes in the band gap (Fig. 2d), by renormalizing the energy gap as dictated by the strain modulation, we account for the impact of the strain field on the energy position of each pair of edge states. As shown in the bottom panel, our calculations reproduces the experimental results. Moreover, dI/dV maps at different energies (see Extended Data in SI Figure S17) reveal that the two pairs of edge states span the bulk energy gap along the perimeters of bilayer islands at 0.5 and 0.6 V. They only emerge along the sharp and straight edges with specific atomic terminations of either Sn or Te atoms, a characteristic observed in both regular and irregular bilayer SnTe structures (see Extended Data in SI Figures S19 and S20).

Since the edge states in our system are protected by time-reversal-mirror symmetry, the second piece of evidence to confirm a 2D TCI is to observe a band gap in the edge states when time-reversal-mirror symmetry is broken. Time-reversal-mirror symmetry can be disrupted spontaneously or through external perturbations such as perpendicular electric field or an in-plane magnetic field²⁰. In contrast with time-reversal symmetry, disorder can always break time-reversal-mirror symmetry. In our effective 3-AL system, intrinsic atomic defects at the edges locally and randomly break the $z \rightarrow -z$ mirror symmetry about the middle plane. As a result, the edge states open up a band gap, as shown in Fig. 3d. The depth of the opened band gap depends on the extent to which mirror symmetry is broken at the edges. Remarkably, we find that the edge states are substantially resilient to the effects of the substrate, the moiré potential, and even a sizable electric field (see Extended Data in SI Figure S15 and S16).

D. Coupling of topological edge states

The interaction of edge states in 3D TCIs has been studied^{23,30}. We probe the possibility of observing coupling between the edge states in our 2D TCI by examining two closely adjacent bilayer islands, as illustrated in Figure 4a. High-resolution topography indicates no significant structural distortions or atomic defects that could disrupt mirror symmetry, so a gap opening in the edge states is not expected. To eliminate the influence of strain, which can shift edge state energy, the tunneling spectra were taken at equivalent points on the same stripe pattern, ensuring a consistent strain field. Our dI/dV spectra reveal that peak 1 shifts to lower energy compared to isolated edges

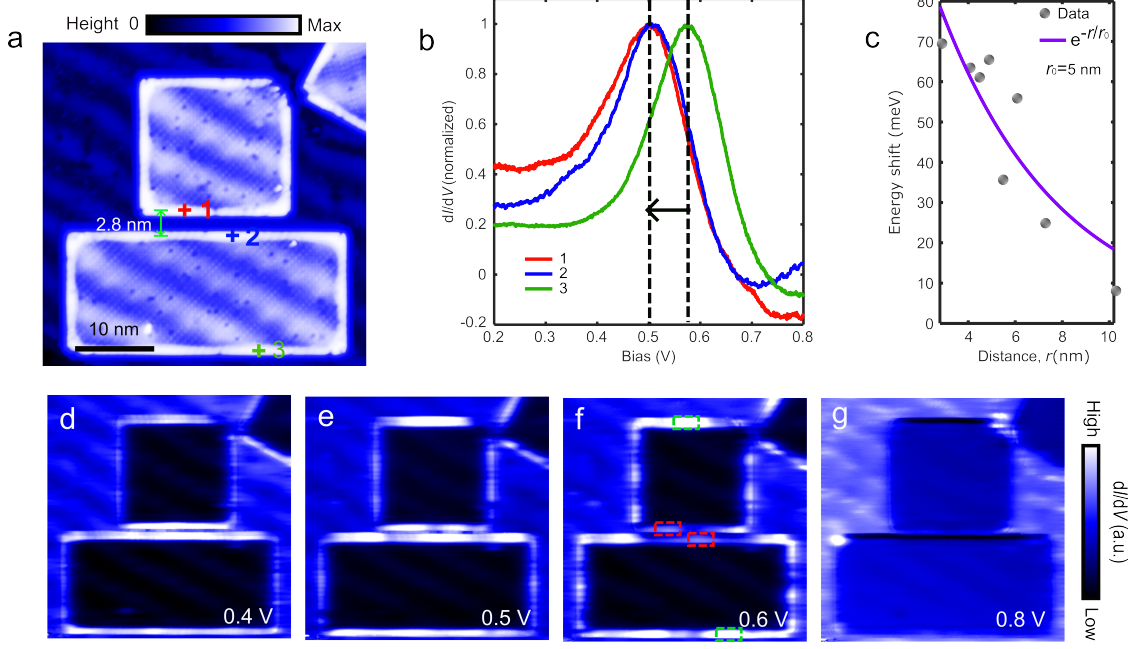


FIG. 4. **Coupling of topological edge channels.** **a**, STM topographic image of two adjacent bilayer SnTe islands ($V_b=0.5$ V, $I=60$ pA). The distance of their neighboring edges is 2.8 nm. **b**, Tunneling spectra taken at the equivalent points 1, 2 and 3 from three edges in **a** by locating the local maximum position of the edge state peaks. The black arrow indicates the shift direction of neighboring edge states. **c**, The blue curve fits the exponential decay of the energy shift of edge states with the increasing distance between two adjacent edges. The decay length is 5 nm. **d-g**, dI/dV maps over the bilayer island from **a** at different bias voltages. The red and green dashed rectangular frames outline the edge states with and without neighboring edges. The tunneling junction setup is $I_{set}=60$ pA.

as indicated by the black arrow (Fig. 4b) and its intensity weakens significantly around 0.6 V. The energy shift due to the proximity of adjacent edges exhibits an exponential decay with increasing distance between the two edges, as seen in Fig. 4c, with a decay length of approximately 5 nm. This effect is most evident in the dI/dV mapping over the bilayer edges at different energies (Figs. 4d-g), as outlined by the green and red rectangular frames.

We propose two possible origins for the energy shift with both expected to coexist in our system. First, we experimentally observe that the edge states shift towards lower energy compared to isolated edges, which can be explained by electrostatic coupling. This type of coupling can alter the energy position of edge states and is sensitive to both the distance between the edges and the strength of the electric field or charge between adjacent edges. Second, there is a possibility of substrate-mediated tunneling between adjacent edges, allowing for interaction through proximity. To assess the magnitude of this effect, we developed a model where the electronic modes in one

bilayer island can tunnel into another island through an effective barrier potential V (details in SI Figure S22). This tunneling coupling leads to a shift of the crossing Dirac point. Comparison with the experimental results is possible by relating V to the distance d between neighboring edges through $\lambda d = \ln\left(\frac{V}{t_0}\right)$, where t_0 is the hopping energy of SnTe orbitals (on the order of eV) and λ is a finite phenomenological parameter that can be adjusted based on experimental data. This model results in an exponential decay of the energy shift as λd increases, consistent with our experimental results. In summary, it is likely that a combination of electrostatic interactions and tunneling coupling is responsible for the energy shift of edge modes for closely spaced SnTe edges.

III. CONCLUSION

In conclusion, we experimentally realized a 2D TCI by artificially constructing a heterostructure of bilayer SnTe on the $2H$ -NbSe₂ substrate. First, we show that this experimental system behaves as an effective strained 3-AL SnTe structure in a compressive regime. *Ab initio* calculations unveil that compressive strain drives this system through a phase transition from a trivial ferroelectric to a crystalline topological insulator that hosts two pairs of edge states protected by time-reversal-mirror symmetry. Second, we employ STM and STS to observe two pronounced peaks associated with the two pairs of edge states within fully gapped bulk states and visualize their propagation along the edges of bilayer islands. Intrinsic atomic defects locally break the time-reversal-mirror symmetry and thus open up a band gap in the edge states. Finally, we show that two closely adjacent topological edge modes can be shifted by a combination of electrostatic interactions and tunneling coupling. Our results establish strain as a powerful control parameter and demonstrate that it can be used to drive few-layer SnTe to a 2D crystalline topological insulator. This crystalline topological phase provides a starting point to potentially engineer Chern insulators by including ferromagnetically ordered dopants^{31–33} or to use this as a building block in van der Waals heterostructures, for example, targeting topological mirror superconductivity^{34,35} by proximity effect.

IV. EXPERIMENTAL METHODS

Ultrathin SnTe films were grown on the freshly cleaved bulk crystal $2H$ -NbSe₂ by molecular beam epitaxy under ultrahigh vacuum conditions (UHV, base pressure $\approx 2 \times 10^{-10}$ mbar). Before the growth, compound material SnTe was fully degassed and $2H$ -NbSe₂ substrate was also out-

gassed at $\sim 100^\circ\text{C}$. During the growth, the SnTe powder of 99.999 % purity loaded into a Knudsen cell was evaporated onto the substrate held at room temperature for 3 minutes. After the growth, the sample was annealed at $\sim 50^\circ\text{C}$. Finally, it was inserted into low-temperature STM head housed in the same UHV system. All the subsequent STM and STS measurements were performed at $T = 4.7\text{ K}$. The etched tungsten tip was used for all the STM scan and electrical measurement. STM images were scanned in the constant-current mode and all the dI/dV spectra were recorded by a standard lock-in techniques while sweeping the sample bias in an open feedback loop configuration, with a peak-to-peak bias modulation of $5\sim 20\text{ mV}$ at a frequency of 746 Hz .

The codes used to extract strain map of bilayer SnTe are based on the available library (<https://github.com/LowTemperaturesUAM/Strain-calculation-from-2D-images>).

V. THEORETICAL METHODS

DFT calculations were realized with the standard Perdew-Burke-Ernzerhof (PBE) functional³⁶ as implemented as in the QUANTUM-ESPRESSO package³⁷. Ultra-soft pseudopotentials from the pslibrary (<https://dalcorso.github.io/pslibrary/>) version 1.0.0 were used to describe the interactions between electrons and ions³⁸, while the wave functions were expanded using a plane-wave basis set with a kinetic energy cutoff of 50 Ry . The integration over the Brillouin zone was performed using a $8\times 8\times 1$ grid. After structural relaxation with the force threshold of 0.01 eV/\AA , all electronic properties were obtained considering spin-orbit coupling with the full-relativistic versions of the same pseudopotentials used previously and Brillouin zone sampling of $10\times 10\times 1$. The Wannier90 package³⁹ was employed to obtain tight-binding Hamiltonians in the basis of maximally localized Wannier functions, including s and p orbitals for both Sn and Te atoms. We fitted the DFT band structures with the tight-binding Hamiltonians considering an energy window of more than 20 eV and a frozen window covering 2 eV .

The same code and pseudopotentials were used to relax and to obtain electronic properties of SnTe/NbSe₂ heterostructures. The Brillouin zone was integrated using a smaller $2\times 2\times 1$ grid, and the vdw-df-ob86 vdW functional was used instead of standard PBE in order to account for weak dispersion interactions that might occur between the layers⁴⁰. All calculations in this part were performed without taking spin-orbit coupling interactions into account.

ACKNOWLEDGEMENTS

This research made use of the Aalto Nanomicroscopy Center (Aalto NMC) facilities and was supported by the European Research Council (ERC-2021-StG No. 101039500 “Tailoring Quantum Matter on the Flatland” and ERC-2017-AdG No. 788185 “Artificial Designer Materials”) and Academy of Finland (Academy Research Fellow No. 331342, No 358088, No. 336243, No. 338478, No. 346654, Academy postdoctoral fellow No. 349696, and the Finnish Quantum Flagship, No. 358877). We acknowledge the computational resources provided by the Aalto Science-IT project.

AUTHOR CONTRIBUTIONS

L.J., M.A., S.K., J.L.L., and P.L. conceived the experiment, and L.J., M.A., carried out the sample growth and the low-temperature STM experiments. L.J., M.A., A.O.F., and O.J.S. analysed the STM data. A.O.F., O.J.S., and J.L.L. developed the theoretical model. L.J., A.O.F., O.J.S., S.K., J.L.L., and P.L. wrote the manuscript with input from all co-authors.

COMPETING INTERESTS

The authors declare no competing interests.

* These authors contributed equally to this work.

† e-mail: kezilebieke.a.shawulienu@jyu.fi; jose.lado@aalto.fi; peter.liljeroth@aalto.fi

- ¹ M. Z. Hasan and C. L. Kane, “Colloquium: Topological insulators,” *Rev. Mod. Phys.* **82**, 3045–3067 (2010).
- ² Xiao-Liang Qi and Shou-Cheng Zhang, “Topological insulators and superconductors,” *Rev. Mod. Phys.* **83**, 1057–1110 (2011).
- ³ Joel E. Moore, “The birth of topological insulators,” *Nature* **464**, 194–198 (2010).
- ⁴ Markus König, Steffen Wiedmann, Christoph Brüne, Andreas Roth, Hartmut Buhmann, Laurens W. Molenkamp, Xiao-Liang Qi, and Shou-Cheng Zhang, “Quantum spin Hall insulator state in HgTe quantum wells,” *Science* **318**, 766–770 (2007), <https://www.science.org/doi/pdf/10.1126/science.1148047>.
- ⁵ Haijun Zhang, Chao-Xing Liu, Xiao-Liang Qi, Xi Dai, Zhong Fang, and Shou-Cheng Zhang, “Topological insulators in Bi₂Se₃, Bi₂Te₃ and Sb₂Te₃ with a single Dirac cone on the surface,” *Nature Physics* **5**, 438–442 (2009).

- ⁶ Y. L. Chen, J. G. Analytis, J.-H. Chu, Z. K. Liu, S.-K. Mo, X. L. Qi, H. J. Zhang, D. H. Lu, X. Dai, Z. Fang, S. C. Zhang, I. R. Fisher, Z. Hussain, and Z.-X. Shen, “Experimental realization of a three-dimensional topological insulator, Bi_2Te_3 ,” *Science* **325**, 178–181 (2009), <https://www.science.org/doi/pdf/10.1126/science.1173034>.
- ⁷ D. Hsieh, Y. Xia, D. Qian, L. Wray, J. H. Dil, F. Meier, J. Osterwalder, L. Patthey, J. G. Checkelsky, N. P. Ong, A. V. Fedorov, H. Lin, A. Bansil, D. Grauer, Y. S. Hor, R. J. Cava, and M. Z. Hasan, “A tunable topological insulator in the spin helical Dirac transport regime,” *Nature* **460**, 1101–1105 (2009).
- ⁸ Ilya K. Drozdov, A. Alexandradinata, Sangjun Jeon, Stevan Nadj-Perge, Huiwen Ji, R. J. Cava, B. Andrei Bernevig, and Ali Yazdani, “One-dimensional topological edge states of bismuth bilayers,” *Nature Physics* **10**, 664–669 (2014).
- ⁹ R. Wu, J.-Z. Ma, S.-M. Nie, L.-X. Zhao, X. Huang, J.-X. Yin, B.-B. Fu, P. Richard, G.-F. Chen, Z. Fang, X. Dai, H.-M. Weng, T. Qian, H. Ding, and S. H. Pan, “Evidence for topological edge states in a large energy gap near the step edges on the surface of ZrTe_5 ,” *Phys. Rev. X* **6**, 021017 (2016).
- ¹⁰ Xiaofeng Qian, Junwei Liu, Liang Fu, and Ju Li, “Quantum spin hall effect in two-dimensional transition metal dichalcogenides,” *Science* **346**, 1344–1347 (2014), <https://www.science.org/doi/pdf/10.1126/science.1256815>.
- ¹¹ Yoichi Ando and Liang Fu, “Topological crystalline insulators and topological superconductors: From concepts to materials,” *Annu. Rev. Condens. Matter Phys.* **6**, 361–381 (2015).
- ¹² Timothy H. Hsieh, Hsin Lin, Junwei Liu, Wenhui Duan, Arun Bansil, and Liang Fu, “Topological crystalline insulators in the SnTe material class,” *Nature Communications* **3**, 982 (2012).
- ¹³ Y. Tanaka, Zhi Ren, T. Sato, K. Nakayama, S. Souma, T. Takahashi, Kouji Segawa, and Yoichi Ando, “Experimental realization of a topological crystalline insulator in SnTe ,” *Nature Physics* **8**, 800–803 (2012).
- ¹⁴ Yoshinori Okada, Maksym Serbyn, Hsin Lin, Daniel Walkup, Wenwen Zhou, Chetan Dhital, Madhab Neupane, Suyang Xu, Yung Jui Wang, R. Sankar, Fangcheng Chou, Arun Bansil, M. Zahid Hasan, Stephen D. Wilson, Liang Fu, and Vidya Madhavan, “Observation of Dirac node formation and mass acquisition in a topological crystalline insulator,” *Science* **341**, 1496–1499 (2013), <https://www.science.org/doi/pdf/10.1126/science.1239451>.
- ¹⁵ Ilija Zeljkovic, Yoshinori Okada, Cheng-Yi Huang, R. Sankar, Daniel Walkup, Wenwen Zhou, Maksym Serbyn, Fangcheng Chou, Wei-Feng Tsai, Hsin Lin, A. Bansil, Liang Fu, M. Zahid Hasan, and Vidya Madhavan, “Mapping the unconventional orbital texture in topological crystalline insulators,” *Nature Physics* **10**, 572–577 (2014).
- ¹⁶ Su-Yang Xu, Chang Liu, N. Alidoust, M. Neupane, D. Qian, I. Belopolski, J. D. Denlinger, Y. J. Wang, H. Lin, L. A. Wray, G. Landolt, B. Slomski, J. H. Dil, A. Marcinkova, E. Morosan, Q. Gibson, R. Sankar, F. C. Chou, R. J. Cava, A. Bansil, and M. Z. Hasan, “Observation of a topological crystalline insulator phase and topological phase transition in $\text{Pb}_{1-x}\text{Sn}_x\text{Te}$,” *Nature Communications* **3**, 1192 (2012).

- ¹⁷ Tian Liang, Satya Kushwaha, Jinwoong Kim, Quinn Gibson, Jingjing Lin, Nicholas Kioussis, Robert J. Cava, and N. Phuan Ong, “A pressure-induced topological phase with large Berry curvature in $\text{Pb}_{1-x}\text{Sn}_x\text{Te}$,” *Science Advances* **3**, e1602510 (2017).
- ¹⁸ Ilija Zeljkovic, Yoshinori Okada, Maksym Serbyn, R. Sankar, Daniel Walkup, Wenwen Zhou, Junwei Liu, Guoqing Chang, Yung Jui Wang, M. Zahid Hasan, Fangcheng Chou, Hsin Lin, Arun Bansil, Liang Fu, and Vidya Madhavan, “Dirac mass generation from crystal symmetry breaking on the surfaces of topological crystalline insulators,” *Nature Materials* **14**, 318–324 (2015).
- ¹⁹ Junwei Liu, Xiaofeng Qian, and Liang Fu, “Crystal field effect induced topological crystalline insulators in monolayer iv–vi semiconductors,” *Nano Letters* **15**, 2657–2661 (2015).
- ²⁰ Junwei Liu, Timothy H. Hsieh, Peng Wei, Wenhui Duan, Jagadeesh Moodera, and Liang Fu, “Spin-filtered edge states with an electrically tunable gap in a two-dimensional topological crystalline insulator,” *Nature Materials* **13**, 178–183 (2014).
- ²¹ Frank Schindler, Zhijun Wang, Maia G. Vergniory, Ashley M. Cook, Anil Murani, Shamashis Sengupta, Alik Yu. Kasumov, Richard Deblock, Sangjun Jeon, Ilya Drozdov, Hélène Bouchiat, Sophie Guéron, Ali Yazdani, B. Andrei Bernevig, and Titus Neupert, “Higher-order topology in bismuth,” *Nature Physics* **14**, 918–924 (2018).
- ²² Josias Langbehn, Yang Peng, Luka Trifunovic, Felix von Oppen, and Piet W. Brouwer, “Reflection-symmetric second-order topological insulators and superconductors,” *Phys. Rev. Lett.* **119**, 246401 (2017).
- ²³ Paolo Sessi, Domenico Di Sante, Andrzej Szczerbakow, Florian Glott, Stefan Wilfert, Henrik Schmidt, Thomas Bathon, Piotr Dziawa, Martin Greiter, Titus Neupert, Giorgio Sangiovanni, Tomasz Story, Ronny Thomale, and Matthias Bode, “Robust spin-polarized midgap states at step edges of topological crystalline insulators,” *Science* **354**, 1269–1273 (2016), <https://www.science.org/doi/pdf/10.1126/science.aah6233>.
- ²⁴ Augusto L. Araújo, Gerson J. Ferreira, and Tome M. Schmidt, “Suppressed topological phase transitions due to nonsymmorphism in snTe stacking,” *Scientific Reports* **8**, 9452 (2018).
- ²⁵ Kai Chang, Thaneshwor P. Kaloni, Haicheng Lin, Amilcar Bedoya-Pinto, Avanindra K. Pandeya, Ilya Kostanovskiy, Kun Zhao, Yong Zhong, Xiaopeng Hu, Qi-Kun Xue, Xi Chen, Shuai-Hua Ji, Salvador Barraza-Lopez, and Stuart S. P. Parkin, “Enhanced spontaneous polarization in ultrathin snTe films with layered antipolar structure,” *Advanced Materials* **31**, 1804428 (2019).
- ²⁶ Kai Chang, Junwei Liu, Haicheng Lin, Na Wang, Kun Zhao, Anmin Zhang, Feng Jin, Yong Zhong, Xiaopeng Hu, Wenhui Duan, Qingming Zhang, Liang Fu, Qi-Kun Xue, Xi Chen, and Shuai-Hua Ji, “Discovery of robust in-plane ferroelectricity in atomic-thick SnTe,” *Science* **353**, 274–278 (2016), <https://www.science.org/doi/pdf/10.1126/science.aad8609>.
- ²⁷ Mohammad Amini, Orlando J. Silveira, Viliam Vaňo, Jose L. Lado, Adam S. Foster, Peter Liljeroth, and Shawulienū Kezilebieke, “Control of molecular orbital ordering using a van der Waals monolayer ferroelectric,” *Advanced Materials* **35**, 2206456 (2023),

<https://onlinelibrary.wiley.com/doi/pdf/10.1002/adma.202206456>.

- ²⁸ Xiaofeng Qian, Liang Fu, and Ju Li, “Topological crystalline insulator nanomembrane with strain-tunable band gap,” *Nano Research* **8**, 967–979 (2015).
- ²⁹ Na Wang, Damien West, Junwei Liu, Jia Li, Qimin Yan, Bing-Lin Gu, S. B. Zhang, and Wenhui Duan, “Microscopic origin of the p -type conductivity of the topological crystalline insulator SnTe and the effect of Pb alloying,” *Phys. Rev. B* **89**, 045142 (2014).
- ³⁰ Johannes Jung, Artem Odobesko, Robin Boshuis, Andrzej Szczerbakow, Tomasz Story, and Matthias Bode, “Systematic investigation of the coupling between one-dimensional edge states of a topological crystalline insulator,” *Phys. Rev. Lett.* **126**, 236402 (2021).
- ³¹ Rui Yu, Wei Zhang, Hai-Jun Zhang, Shou-Cheng Zhang, Xi Dai, and Zhong Fang, “Quantized anomalous hall effect in magnetic topological insulators,” *Science* **329**, 61–64 (2010).
- ³² Chen Fang, Matthew J. Gilbert, and B Andrei Bernevig, “Large-charge-number quantum anomalous hall effect in thin-film topological crystalline insulators,” *Phys. Rev. Lett.* **112**, 046801 (2014).
- ³³ B. Andrei Bernevig, Claudia Felser, and Haim Beidenkopf, “Progress and prospects in magnetic topological materials,” *Nature* **603**, 41–51 (2022).
- ³⁴ Fan Zhang, C. L. Kane, and E. J. Mele, “Topological mirror superconductivity,” *Phys. Rev. Lett.* **111**, 056403 (2013).
- ³⁵ Liang Fu and C. L. Kane, “Superconducting proximity effect and majorana fermions at the surface of a topological insulator,” *Phys. Rev. Lett.* **100**, 096407 (2008).
- ³⁶ John P. Perdew, Kieron Burke, and Matthias Ernzerhof, “Generalized gradient approximation made simple,” *Phys. Rev. Lett.* **77**, 3865–3868 (1996).
- ³⁷ Paolo Giannozzi, Stefano Baroni, Nicola Bonini, Matteo Calandra, Roberto Car, Carlo Cavazzoni, Davide Ceresoli, Guido L Chiarotti, Matteo Cococcioni, Ismaila Dabo, Andrea Dal Corso, Stefano de Gironcoli, Stefano Fabris, Guido Fratesi, Ralph Gebauer, Uwe Gerstmann, Christos Gougoussis, Anton Kokalj, Michele Lazzeri, Layla Martin-Samos, Nicola Marzari, Francesco Mauri, Riccardo Mazzarello, Stefano Paolini, Alfredo Pasquarello, Lorenzo Paulatto, Carlo Sbraccia, Sandro Scandolo, Gabriele Sclauzero, Ari P Seitsonen, Alexander Smogunov, Paolo Umari, and Renata M Wentzcovitch, “Quantum espresso: a modular and open-source software project for quantum simulations of materials,” *Journal of Physics: Condensed Matter* **21**, 395502 (2009).
- ³⁸ Andrea Dal Corso, “Pseudopotentials periodic table: From h to pu,” *Computational Materials Science* **95**, 337–350 (2014).
- ³⁹ Giovanni Pizzi, Valerio Vitale, Ryotaro Arita, Stefan Blügel, Frank Freimuth, Guillaume Géranton, Marco Gibertini, Dominik Gresch, Charles Johnson, Takashi Koretsune, Julen Ibañez-Azpiroz, Hyungjun Lee, Jae-Mo Lihm, Daniel Marchand, Antimo Marrazzo, Yuriy Mokrousov, Jamal I Mustafa, Yoshiro Nohara, Yusuke Nomura, Lorenzo Paulatto, Samuel Poncé, Thomas Ponweiser, Junfeng Qiao, Florian Thöle, Stepan S Tsirkin, Małgorzata Wierzbowska, Nicola Marzari, David Vanderbilt, Ivo Souza, Arash A Mostofi, and Jonathan R Yates, “Wannier90 as a community code: new features and applications,”

Journal of Physics: Condensed Matter **32**, 165902 (2020).

- ⁴⁰ Jiří Klimeš, David R. Bowler, and Angelos Michaelides, “Van der waals density functionals applied to solids,” *Phys. Rev. B* **83**, 195131 (2011).